
Region of freshwater influence (ROFI) and its impact on sediment transport in the lower Mekong Delta coastal zone of Vietnam

Nguyen Nguyet-Minh ¹, San Dinh Cong ¹, Nguyen Kim Dan ², Pham Quoc Bao ³,
Gagnon Alexandre S. ⁴, Mai Son T. ⁵, Anh Duong Tran ^{6,*}

¹ Southern Institute of Water Resources Research, Ho Chi Minh City, Vietnam

² Laboratory for Hydraulics Saint-Venant, Université Paris-Est, 6 Quai Wattier, 78400, Chatou, France

³ Faculty of Natural Sciences, Institute of Earth Sciences, University of Silesia in Katowice, Będzińska street 60, 41-200, Sosnowiec, Poland

⁴ School of Biological and Environmental Science, Liverpool John Moores University, Liverpool, L3 3AF, UK

⁵ School of Electronics, Electrical Engineering and Computer Science, Queens University, Belfast, UK

⁶ HUTECH University, 475A Dien Bien Phu Street, Binh Thanh District, Ho Chi Minh City, Vietnam

* Corresponding author : Duong Tran Anh, email address : ta.duong@hutech.edu.vn

Abstract :

The delta of the Mekong River is one of the largest in the world, with the Mekong River carrying a large amount of sediments in its Region of Freshwater Influence (ROFI). This study investigates the flow structure and movement of both suspended and bedload sediments in the ROFI of the Lower Mekong Delta (LMD) in order to identify areas prone to sediment accretion and erosion. This is accomplished by applying the three-dimensional Coastal and Regional Ocean COmmunity (CROCO) model and then calculating the sediment budget of different stretches of the coastline. The model outputs, depicting areas experiencing sediment accretion and erosion along the coastline of the LMD, are then compared against observations obtained during the period 1990–2015 and demonstrate the ability of the model to identify areas particularly prone to erosion and where preventive actions against coastal erosion should focus.

Keywords : Accretion and erosion, CROCO model, ROFI, Sediment transport, Mekong Delta

27 **1. Introduction**

28 The Mekong Delta in southern Vietnam hosts a population of over 17 million people
29 ([Buschmann et al., 2008](#)). It is an important region for agriculture and aquaculture, producing
30 over 55% of the rice crop of the country and over 60% of its seafood ([Guong and Hoa, 2012](#)),
31 in addition to being a hotspot of biodiversity, the second in the world after the Amazon basin
32 ([Ziv et al., 2012](#); [Campbell, 2012](#)). The Mekong Delta region, however, is facing many
33 challenges such as an expansion of hydropower development across the Mekong River Basin,
34 which has led to a significant reduction to the supply of sediments entering the delta ([Cochrane](#)
35 [et al., 2014](#); [Kondolf et al., 2014](#)), causing coastal erosion ([Li et al., 2017](#); [Le Xuan et al.,](#)
36 [2019](#)),

37

38 The Mekong is among the largest rivers worldwide; the eighth largest river in terms of its
39 discharge and the tenth most important for its sediment load ([Meade, 1996](#); [Li et al., 2017](#)). The
40 average annual discharge of the Mekong River is approximately 12,500 m³/s, although it
41 experiences strong seasonal variations, with a ratio of maximum to minimum discharge in a
42 year of around six to eight. This volume of freshwater contributes to an important and
43 seasonally variable buoyancy plume to an extensive region of its coastal zone and adjacent shelf
44 sea, a region referred to as the Region of Freshwater Influence (ROFI) ([Simpson, 1997](#)). The
45 ROFI can extend offshore from one kilometre from the Mekong River estuary to several
46 hundred kilometres depending on the magnitude of the river discharge ([Geyer & Kineke, 1995](#);
47 [Horner-Devine et al., 2015](#)).

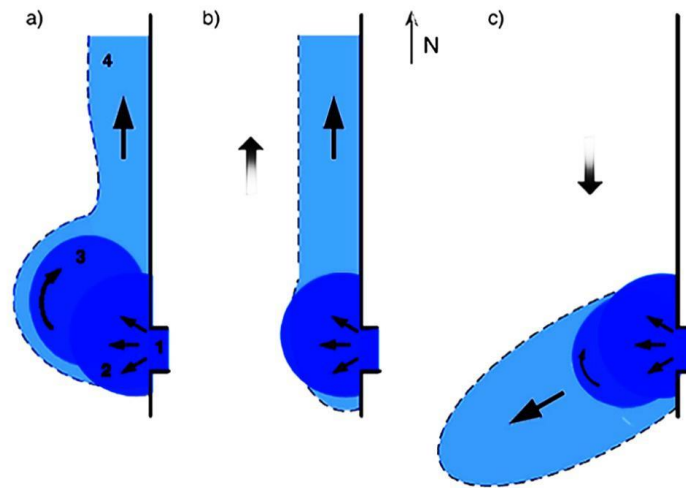
48

49 The ROFI of many coastal regions worldwide has previously been investigated, but with a
50 limited number of studies focusing on the Mekong Delta ([Fong & Geyer, 2002](#); [De Boer et al.,](#)
51 [2006](#)). Both estuarine and shelf sea processes take place in a ROFI ([Simpson, 1997](#); [Horner-](#)
52 [Devine et al., 2015](#)), with the amount of mixing in the ROFI depending on wind speed and

53 direction, tidal range, the shape of the estuary and the amount of river discharge. The ROFI of
54 the Mekong Delta thus strongly varies seasonally, depending mainly on the monsoonal winds
55 and the magnitude of the Mekong River discharge (Hordoir *et al.*, 2006), as the Coriolis force
56 is weak at the latitude of the delta (Simpson and Snidvongs, 1998).

57

58 Horner-Devine *et al.* (2009) proposed the following conceptual model of the ROFI. At very low
59 wind speeds, freshwater flows out of the river mouth to form a two-part structure: a baroclinic
60 recirculation bulge near the river mouth and a coastal current. In this situation, the freshwater
61 bulge experiences an anticyclonic circulation and grows indefinitely until altered by an external
62 force such as an ambient current or wind (Figure 1a). When the winds are strong enough, the
63 freshwater plume is influenced by Ekman transport (Price *et al.*, 1987; Wang *et al.*, 2013).
64 Upwelling and downwelling can occur during a tidal cycle as well as on a seasonal scale due to
65 changing monsoon winds (Chen *et al.*, 2012; Hein *et al.*, 2013). Downwelling winds blowing
66 towards the coastline impact the plume dynamics by compressing it against the coast (Figure
67 1b), while upwelling winds blowing across the ocean surface cause expansion of the freshwater
68 plume sea-ward and detachment of the low salinity water from the plume, erasing the buoyancy
69 signature (Figure 1c). This is because the movement of the freshwater plume offshore due to
70 Ekman transport causes the intrusion of saltier ambient waters on the continental shelf,
71 promoting plume detachment and leaving mixed waters near the coast (Pimenta *et al.*, 2011;
72 Joseph, 2017).



73

74 **Figure 1.** Conceptual model of a ROFI under three different wind forcing conditions: a)
 75 freshwater plume during low wind speeds, with numbers 1, 2, 3, and 4 showing the river
 76 (source), tidal, bulge, and the far-field parts, respectively, of the river plume; b) freshwater
 77 plume under downwelling conditions, which compress the re-circulating and far-field plumes
 78 against the coast; and c) freshwater plume under upwelling conditions (adapted from [Horner-](#)
 79 [Devine et al. 2009](#)).

80

81 Previous studies have investigated the dynamics of river plumes and the ROFI using either
 82 laboratory experiments ([Thomas & Linden, 2010](#); [Yuan et al., 2018](#)), field measurements
 83 ([Geyer et al., 2004](#); [Simpson et al., 2005](#)) or numerical models ([Whitney & Garvine, 2005](#);
 84 [Xing & Chen, 2017](#)). These studies, nonetheless, have to date mainly focused on the structure
 85 and dynamics of the freshwater bulge and coastal currents with limited attention paid to
 86 salinity variations and sediment transport due to seasonal changes in monsoonal wind ([Yao et](#)
 87 [al., 2016](#)). In that regard, the deposition of fine sediments on the continental shelf during the
 88 Southwest (SW) monsoon due to high river discharge has been demonstrated ([Thanh et al.,](#)
 89 [2017](#); [Le Xuan et al., 2019](#)). However, previous studies have also suggested that sediment
 90 deposition occurs during the low flow season, but it is limited to areas near the river mouth,
 91 where the delta is still expanding, and that the wind driven circulation, waves, and tidal action
 92 cause net erosion in other parts of the Lower Mekong Delta Coastal Zone (LMDCZ) during

93 that season. Even though the net transport of fine sediments at the annual time-scale is to the
94 south, i.e., towards the Gulf of Thailand, there is a negative sediment budget on the coast of
95 that region due to the strong coastal current causing coastal erosion and hence shoreline retreat,
96 evidence for which is presented in [Karlsruud et al. \(2017\)](#). This strong coastal current, flowing
97 in the direction of the propagating Kelvin wave, was also observed in the modelling study of
98 [Hordoir et al. \(2006\)](#) mentioned earlier.

99

100 In brief, [Hordoir et al. \(2006\)](#) identified the main processes of the freshwater plume under
101 seasonally varying monsoonal winds, river flow regimes and salinity profiles, but without
102 considering sediment transport, while [Hein et al. \(2013\)](#) investigated the influence of seasonal
103 variations in river discharge and monsoonal winds on the dynamics of suspended sediments,
104 but not that of bedload sediments. [Marchesiello et al. \(2019\)](#), for their part, previously applied
105 the CROCO model to the Mekong Delta to investigate sediment dynamics and the associated
106 shoreline change, but they did not consider the influence of seasonal variability in salinity, flow
107 structure and their impact on sediment transport in the ROFI. Besides, [they](#) mentioned the
108 importance of considering the re-suspension of sediments caused by the action of waves on the
109 seabed, particularly during the north-easterly winds in the winter, and their subsequent
110 distribution by ocean currents. Studies in other regions have also shown that the ROFI
111 influences not only the transport of suspended sediments but also that of bedload sediments.
112 Therefore, an investigation of the processes and dynamics of the ROFI incorporating sediment
113 transport is recommended in view of recent anthropogenic changes in the basin.

114

115 This study aims to improve our knowledge of the structure of the ROFI in the Mekong Delta
116 and its impact on the regional coastal ocean circulation and sediment transport using a three-
117 dimensional model that takes into consideration different forcings, namely the outflow of
118 freshwater from rivers into the estuary, the tides, waves, winds, and the Coriolis force, even

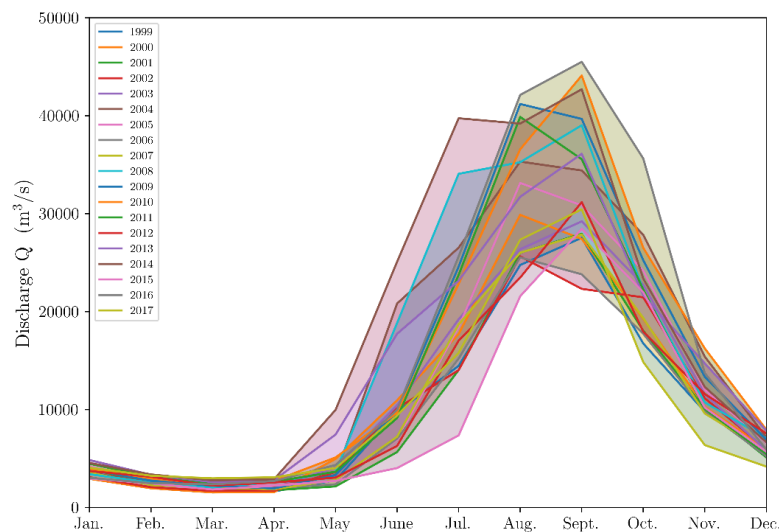
119 though the latter is considered to be minor at the latitude of the study region. By simulating the
120 movement of both suspended and bedload sediments, this modelling study also aims to identify
121 areas prone to sediment accretion and erosion by establishing an updated sediment budget
122 along stretches of the coastline, in view of recent anthropogenic changes in the basin, and to
123 compare that sediment budget with long-term observations.

124

125 2. Methodology

126 2.1. Hydrological, sediment and salinity data

127 **Figure 2** depicts the annual cycle of the discharge of the Mekong River at Kratie in Cambodia
128 over a 45-year period extending from 1999 to 2017. The Mekong Delta is located in a tropical
129 climate region dominated by two seasons defined primarily on the basis of precipitation: a wet
130 season typically lasting from June to October, a cool and dry season, and two transition periods
131 from mid-March to mid-May and in October. Accordingly, the highest discharge is typically
132 reached during the South-west monsoon in August-September, which encourages coastal
133 upwelling. This is in contrast to the cool and dry months of November to February when North-
134 easterly winds dominate the region, promoting downwelling events.



135

136 **Figure 2.** Annual cycle of the Mekong river discharge at Kratie (Cambodia) for all years
137 during the period 1999-2017

138

139 Data from two field surveys of 15 days each, one in October 2016 and the other in February-
140 March 2017, conducted as part of the LMDCZ project (SIWWR, 2018), were obtained to
141 validate the model, as described below. During each field survey, two hydrological stations
142 were set up: Go Cong and U Minh (see Figure 1A in the Appendix), and these were
143 supplemented by 183 measurement points taken using two ships, which sailed from Tien
144 Giang on the northern shore of the Mekong River and Kien-Giang in the Gulf of Thailand to
145 Ca-Mau Cape. Data to calculate the significant wave heights and current velocity were
146 collected every 15 minutes at Go Cong and U Minh using FlowQuest Acoustic Current
147 Profilers, while Suspended Particles Matters (SPM) and salinity was measured at the ship
148 measurement points, with one measurement taken at the following depth: 0.2H, 0.4H, 0.6H,
149 0.8H, where H is the total water depth (m), and on the sea floor using water sample bottles.
150 Each set of measurement lasted 30 minutes.

151 2.2. Coastal and Regional Ocean Community Model

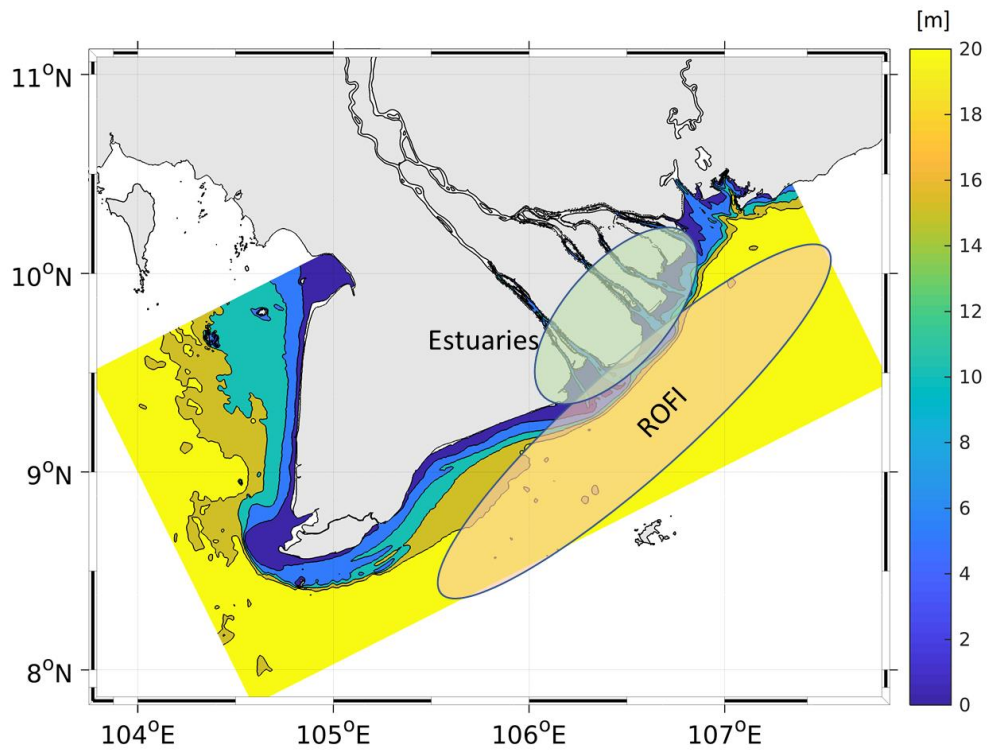
152 This study uses version 1.1 of the CROCO model (<https://www.croco-ocean.org/>), a French
153 model building on the Regional Oceanic Modelling System (ROMS) (Dong *et al.*, 2021). The
154 model solves the primitive equations based on the Boussinesq approximation and the
155 hydrostatic hypothesis (Shchepetkin & McWilliams, 2005; Debreu *et al.*, 2012). It is
156 discretised in geometry, following the curvilinear mesh, with short time steps used to advance
157 the surface elevation and 2D momentum, and larger time steps for solving the 3D momentum
158 equations and the transport equations of scalar variables, i.e., temperature, salinity, and
159 sediment concentration. A third order predictor-corrector algorithm is developed in the code,
160 allowing for a substantial increase in the time step for an efficient integration of realistic
161 configurations of the computational domain, even using fine meshes. A non-local, K-Profile
162 Planetary (KPP) boundary layer scheme (Large *et al.*, 1994) parameterises the unresolved
163 physical vertical sub grid-scale processes, with specific treatment for surface and bottom

164 boundary layers in shallow water. An active, implicit, upstream-biased radiation condition is
165 used at open-ocean boundaries (Marchesiello *et al.*, 2001). CROCO also includes an accurate
166 pressure gradient algorithm (Shchepetkin & McWilliams, 2003). The hydrodynamic model is
167 therefore developed to simulate both coastal and oceanic regions and their interactions with a
168 high degree of accuracy (Debreu *et al.*, 2016; Soufflet *et al.*, 2016), and is coupled with
169 sediment dynamics from Blaas *et al.* (2007) and Warner *et al.* (2008) to compute sediment
170 transport, erosion, and deposition.

171 **3. Model setup**

172 **3.1 Model geometry**

173 The model bathymetry was generated by merging datasets covering the main distributaries,
174 estuaries, and coastal areas using *in situ* measurements and bathymetric data from the General
175 Bathymetric Chart of the Oceans (GEBCO, 2014) at a horizontal resolution of 30 arc-seconds
176 (Figure 3). This domain covers over 744 km of the LMD coastline from Xoai Rap Bay in the
177 Northeast to Ha Tien in the Northwest. The sea open boundaries are located approximately
178 150-200 km from the coastline at Go Cong and U Minh. The horizontal grid resolution is
179 approximately 500 m, which is less than the Rossby radius in the coastal zone (Hordoir *et al.*,
180 2006), with 30 sigma layers in the vertical. An initial attempt was also made to use a 10-layer
181 vertical grid to minimise computational time, as described in SIWRR (2018), but the results
182 were not as conclusive and, for this reason, this present paper increase to a 30-layer vertical
183 grid.



184

185 **Figure 3.** Bathymetry of the study domain with a schematic representation of the ROFI of the
 186 Mekong delta and adjacent shelf sea

187 **3.2 Parameterization**

188 Sediment transport was modelled using the multi-class community model embedded within
 189 ROMS, which accounts for the influence of waves on sediment transport as well as the
 190 interactions between waves and tidal currents. Wave heights were considered in the model by
 191 using empirical formulae for wave dissipation and the wave outputs from the ERA-Interim
 192 reanalysis. The model followed a multi-class sediment approach and based on laboratory
 193 analyses of suspended and bedload sediments collected during field surveys, two classes
 194 needed to be considered: silt with a median diameter of 20 μm and a settling velocity of 0.03
 195 mm/s, and sand with a median diameter of 200 μm and a settling velocity of 20 mm/s. The
 196 model has a horizontal resolution of 500 m (374x727 pts) and a 30-layers in the vertical
 197 (terrain following). [Table 1](#) presents the model configuration variables and their sources
 198 including river, tidal, wave and air-sea forcing and sediment parameters.

199

Table 1. Model configuration variables and their sources

| Parameters | | Data source |
|---------------------|-----------------------------------|---------------------------------------------------------------------------------------------------------------------------------------------------------------------------|
| Topography | | Southern Institute of Water Resources Research (SIWRR) data (estuaries, nearshore area) + GEBCO_2014 at 30" (1km) |
| River forcing | Q, SSC | Discharge and SSC at Can Tho and My Thuan from SIWRR station data |
| Tidal forcing | u, v, SSH | OSU TPXO8 global solution at 1/30° (~3 km) |
| Subtidal forcing | u, v, SSH, T, S, SSC | ECCO V2 reanalysis 1/4° 3-daily |
| Air-sea forcing | wind, heat, and freshwater fluxes | ECMWF ERA-Interim at 1/4° 6-hourly |
| Wave forcing | Hs, Dir, Tp | ECMWF ERA-Interim at 1/4° 6-hourly; for very shallow areas, the wave height data were modulated using an empirical model of wave dissipation proposed by Grosskopf (1980) |
| Sediment parameters | D ₅₀ , W _s | Sand: d ₅₀ =200 μm; W _s =20-50 mm/s Mud (Flocules): d ₅₀ =20 μm; W _s =0.03 mm/s |

200 SSH denotes the sea surface height; U and V are the zonal and meridional velocities, respectively; Hs;
201 wave height; Tp: wave period; Dir: wave direction; SSC: suspended sediment concentration, T:
202 temperature, S: salinity, D₅₀: particle diameter at 50% in the cumulative distribution, W_s: Sediment
203 velocity.

204

205

206 3.3 Boundary conditions

207 The computational domain used for the application of the Coastal and Regional Ocean
208 COmmunity (CROCO) model used upstream discharges at My Thuan on the Tien River and
209 Can Tho on the Hau River, as upstream boundaries, both located about 100 km from the sea.

210 The tidal boundary conditions were obtained from the TPXO-atlas, while the Estimating the
211 Circulation and Climate of the Ocean (ECCO) reanalysis provided the ocean circulation
212 conditions, including baroclinic forcing (i.e., temperature and salinity). The ECMWF ERA-
213 Interim global reanalysis was used to provide atmospheric forcing to run the model, i.e., the

214 total net heat flux and wind stress. The suspended sediment concentration, as measured at Can
215 Tho and My Thuan during 2016-2017, were used as upstream boundary conditions.

216 **4. Model validation**

217 To develop a conceptual structure of the ROFI in the Mekong Delta, the model, after the
218 validation described below, was used to simulate the estuarine and coastal circulations,
219 saltwater intrusion during high tides and sediment transport for the year 2014 using data on the
220 bathymetry, the atmospheric conditions, and the state of the sea (i.e., waves, wind, tidal
221 current). Nonetheless, a longer simulation over a period of two to three years would be
222 preferable to consider the fate of sediments beyond one year, i.e., their deposition, re-
223 suspension, and movement, and research is currently underway to account for this.

224

225 Model validation for the significant wave heights at Go Cong during the two field campaigns
226 illustrates a similar comparison for the current velocity at the surface and at the bottom of the
227 sea (see [Figure 2A](#)) with [Table 2](#) presenting the level of agreement between the model outputs
228 and the observations using different statistical measures. The correlation between the model
229 simulation and the observations is highest for significant wave height than for velocity, and the
230 correlation (error) was higher (lower) for velocity at U Minh than at Go Cong ([Figure 3A](#)).

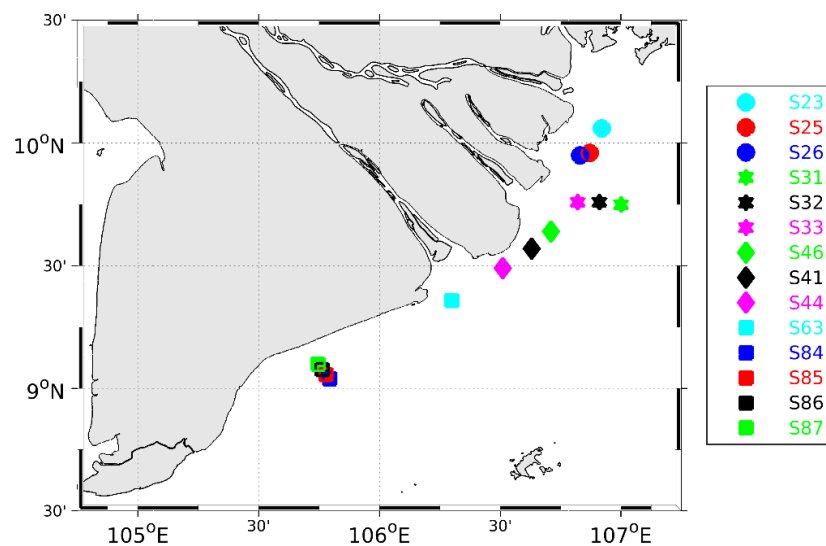
231 The CROCO model was also validated using salinity and SPM concentrations measurements
232 taken using a Conductivity, Temperature and Depth (CTD) package of electronic measurements
233 and an Acoustic Doppler Current Profiler (ADCP), respectively, during the two field campaigns
234 mentioned above and field data collected as part of the *Vietnam TELédétection remote sensing*
235 (VITEL) project ([IRD, 2014](#)) in June 2014 (see [Figure 4](#)).

236 **Table 2.** Model performance at the two stations

| Parameters and stations | RMSE | MAE | R ² |
|-------------------------|------|-----|----------------|
|-------------------------|------|-----|----------------|

| | | | |
|-------------------------------------------------------|----------|----------|------|
| Significant wave heights in Oct. 2016 at Go-Cong | 0.17 m | 0.14 m | 0.61 |
| Significant wave heights in Feb.-Mar. 2017 at Go-Cong | 0.17vm | 0.14 m | 0.49 |
| Surface velocity in Feb.-Mar. 2017 at U-Minh | 0.07vm/s | 0.05 m/s | 0.35 |
| Bottom velocity in Feb.-Mar. 2017 at U-Minh | 0.05 m/s | 0.05 m/s | 0.35 |
| Surface velocity in Feb.-Mar. 2017 at Go-Cong | 0.18 m/s | 0.14 m/s | 0.21 |
| Bottom velocity in Feb.-Mar. 2017 at Go-Cong | 0.16 m/s | 0.13 m/s | 0.22 |

237 RMSE: Root Mean Square Error; MAE: Mean Absolute Error, R^2 : coefficient of determinant



238

239 **Figure 4.** Locations of the salinity profiles and SPM measured by CTD during the VITEL
 240 (IRD, 2014) and LMDCZ projects (SIWWR, 2018)

241

242 The good agreement of vertical salinity distribution and SPM concentration between measured
 243 and simulated results are shown in Figure 4, 5, 6A in the Appendix. Figure 4A and 5A show
 244 that the modelled simulation of the salinity profiles compares well with the CTD measurements
 245 taken at the different locations. Moreover, these salinity profiles clearly reveal the presence of
 246 the ROFI as thin layers of low salinity are observed in the upper part of the vertical profile (less
 247 than 5 m from the surface) at some locations, particularly in June when the discharge from the

248 Mekong River is high due to the rainy season driven by the SW monsoon. [Figure 5A](#), for its
249 part, shows that during the dry season (February-March), the haloclines are weaker and almost
250 non-existent at some locations.

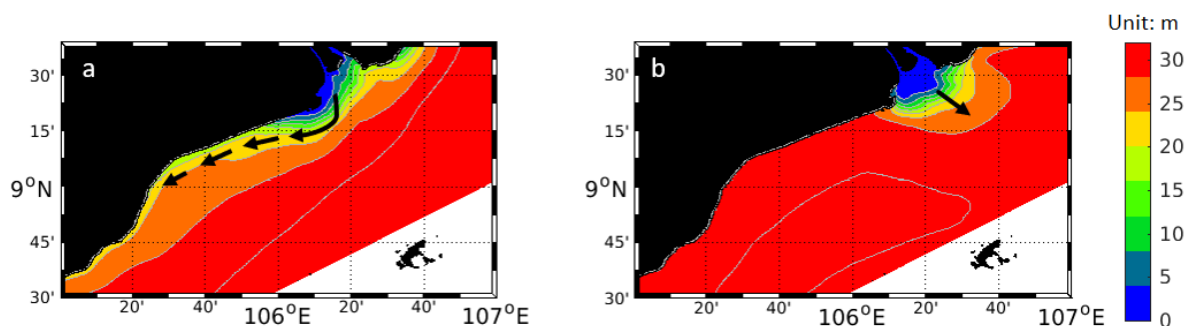
251

252 The instantaneous profiles of the computed SPM with the measured ones at a number of stations
253 were shown in [Figure 6A](#). Because the SPM samplings for a vertical profile last 30 minutes,
254 the values measured at different depths of a profile could be not simultaneous. For this reason,
255 a qualitative comparison was preferred for this variable rather than a quantitative one. In
256 general, it is observed that the difference between the simulated and observed SPM is larger at
257 greater depths, refer to S26 and S41 in particular. The simulated SPM is overestimated in
258 comparison to the observed SPM at S31 while it is underestimated at S26 and S41.

259

260 [Figure 5](#) shows the freshwater plume, as simulated by the model, during two different wind
261 regimes in 2014: winds encouraging downwelling in January and winds promoting upwelling
262 in July. The shape of the plumes agrees very well with the conceptual model presented in
263 [Figure 1](#), i.e., during the dry period extending from November to February, the freshwater
264 outflow from the Hau River forms a bulge near the river mouth of limited outward extent and
265 a narrow current alongside the coast, as the downwelling conditions compress the current
266 against the coast. In July during the rainy season, however, the strong river discharge and the
267 upwelling wind conditions promote offshore development of the plume.

268



269 **Figure 5.** Monthly average freshwater plume at the mouth of the Hau River during the
270 January downwelling winds (left) and the July upwelling winds (right) in 2014.

271

272

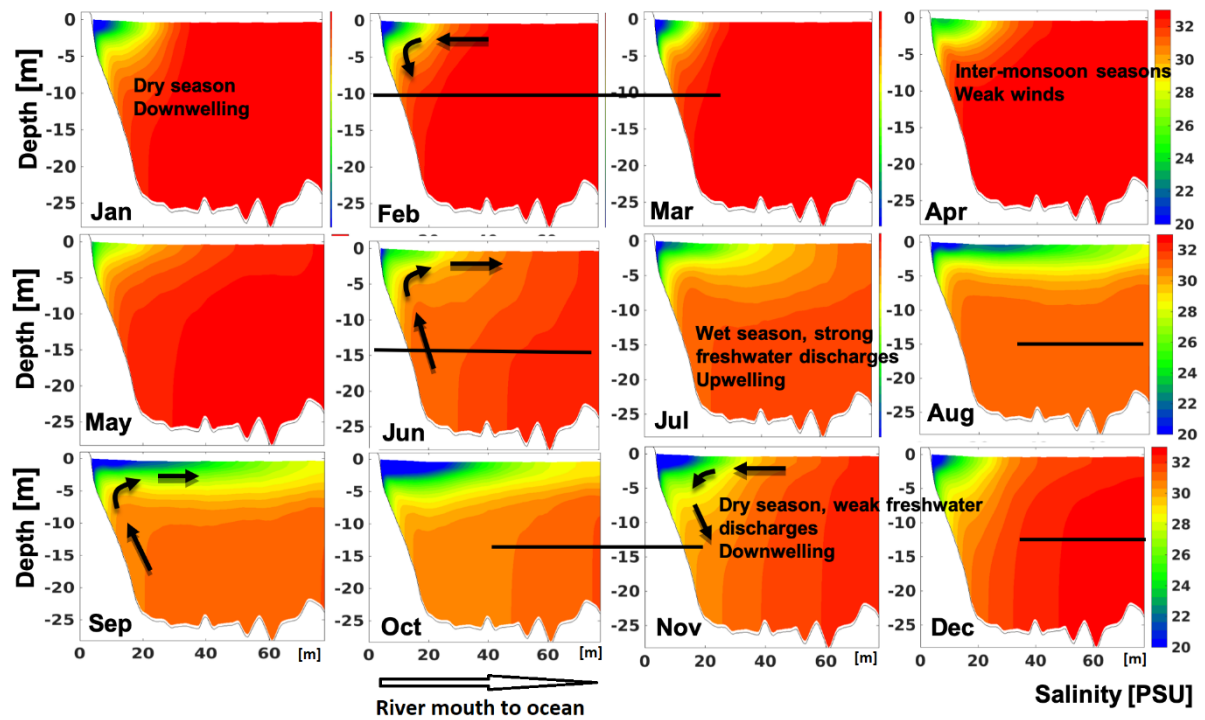
273 **5. Results and discussion**

274 **5.1. Seasonal variability in salinity in the ROFI of the LMDCZ**

275 [Figure 6](#) depicts seasonal variations in the spatial extent of the buoyancy plume during 2014 at
276 Cross-Section CS₃ opposite the mouth of the Hau River at Dinh An and Tran De for the
277 location). From June to the first two weeks of October, the river plume extends 70-90 km
278 offshore because of the large river discharge during the rainy season. This plume creates strong
279 stratification with an approximately 5 m thick freshwater layer, and also contributes to the
280 buoyancy input of the adjacent shelf sea, generating a strong horizontal gradient in salinity.
281 This induces a density-driven circulation with the freshwater at the surface moving offshore
282 and the denser saltwater at the bottom moving shoreward.

283

284 [Hordoir *et al.* \(2006\)](#) previously modelled the freshwater plume of the Mekong River to
285 examine its characteristics. The river plume of the Mekong River exhibits strong variability,
286 because of high seasonal variability in river flow and the monsoonal winds ([Hein *et al.*, 2013](#)).
287 The major physical processes in the ROFI can be described by the basic competition between
288 buoyancy and stirring, with the latter occurring mainly as a result of wind and tidal motions.
289 From the last two weeks of October to mid-March, north-easterly winds favouring downwelling
290 take place. Freshwater at the surface is directed back towards the coast and forced to sink. The
291 plume extends southward upon leaving the estuaries because of the Coriolis force, and then
292 forms a narrow but strong southward current propagating along the coast as a boundary-trapped
293 Kelvin wave.



294

295 **Figure 6.** Monthly average salinity profile at cross-section CS₃ for the year 2014.

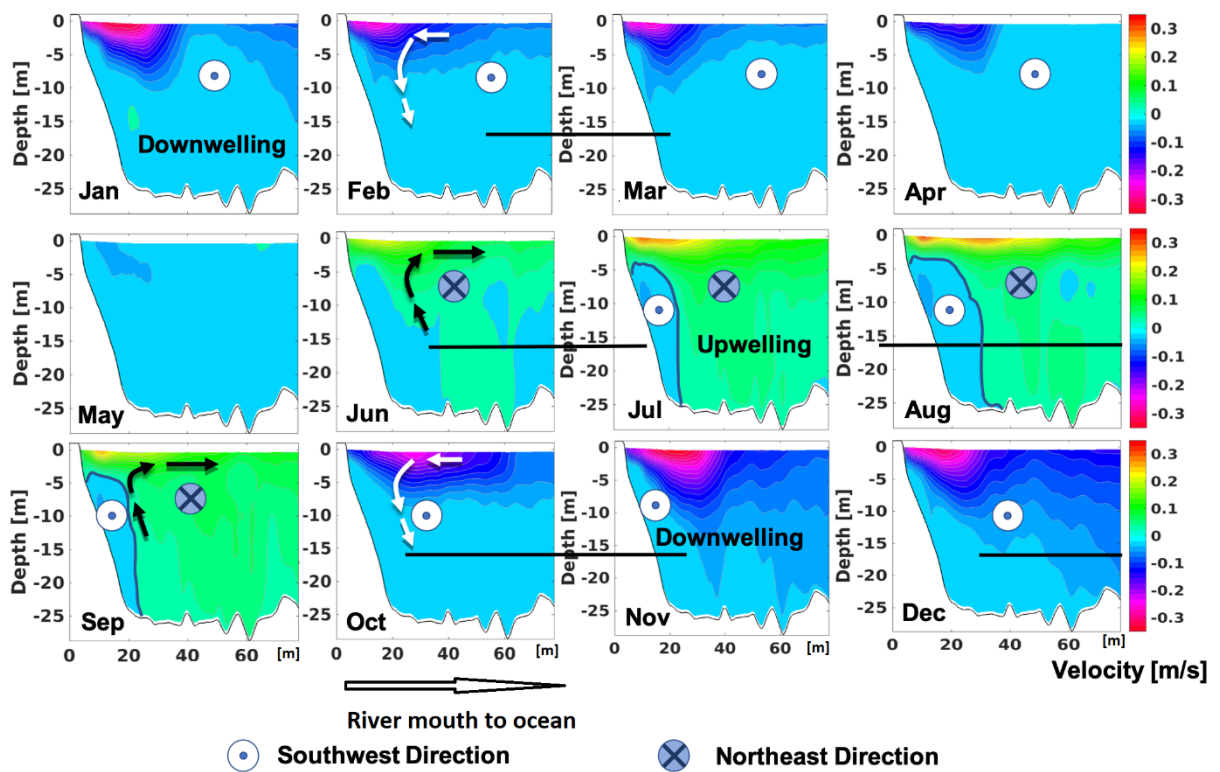
296 **5.2. Flow structure in the ROFI of the Mekong delta**

297 [Figure 7](#) depicts the monthly average longshore current velocities at CS₃. During the wet
 298 season, due to the south-western winds that are favourable to upwelling, large volumes of
 299 freshwater flow out of the mouth of the rivers of the Mekong Delta, creating a stratified plume
 300 extending offshore in a south-easterly direction. [Figure 7 and 8](#) further show that in proximity
 301 to the coast, the longshore currents are in the direction opposite to those of the surface. These
 302 south-westerly bottom currents occupy an area extending vertically from the seabed to 5 m
 303 from the surface, and horizontally from the coast up to 30 km offshore ([Figure 6](#)).

304

305 During the dry season, from mid-October to March, due to the winds from the Northeast
 306 promoting downwelling, the freshwater plume is squeezed in a narrow coastal jet about 25-40
 307 km wide and 5-7 m thick flowing in a south-westerly direction. This surface coastal jet is most
 308 developed in November, when the North-easterly winds are most intense, reaching a velocity
 309 of 0.50 m/s and allowing the transport of suspended sediments along the East Coast of Vietnam

310 in a southerly direction up to Ca Mau Cape, and subsequently carrying them into the West Sea.



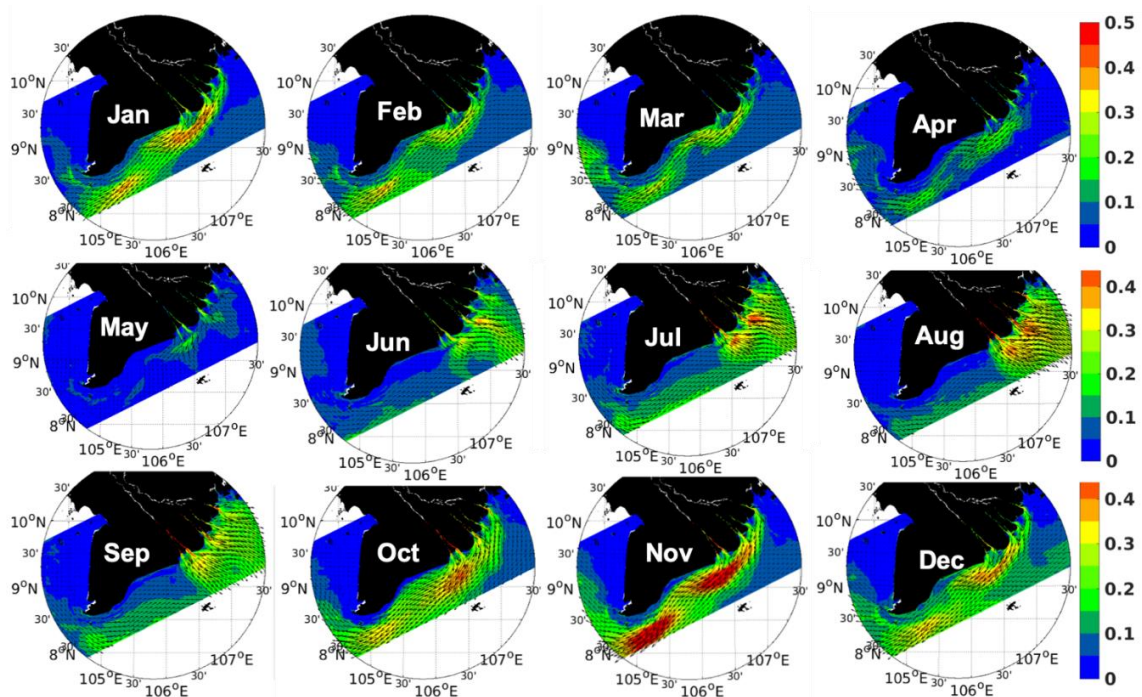
311

312 **Figure 7.** Mean monthly longshore current velocity at CS₃. Negative and positive values refer
313 to South-westerly and North-easterly winds, respectively.

314

315 [Figures 8 and 9](#) present the monthly average velocity fields on the surface and at the
316 bottom, respectively, for the year 2014. It reaches maximum level both in intensity (highest
317 velocity) and in extension (largest occupied area) in August and then reduces in intensity and
318 size in September. At the same time, in proximity to the mouth of the Mekong Delta, the
319 bottom currents are opposite to the surface ones, i.e., seawaters flow back to the estuaries.
320 From the last two weeks of October, north-easterly winds, favourable to downwelling,
321 transport surface waters back to the shore. As above, this jet is strongest and extends until the
322 Ca Mau Cape in November. Its intensity reduces in December and reaches its lowest value in
323 April. The bottom currents during the north-easterly winds are in the same direction as the
324 surface ones, but of weaker intensity. [Figure 10](#) provides a schematic representation
325 summarising the flow structure in the LMDCZ on the basis of the model simulations. The

326 surface and bottom currents are strongly influenced by the wind direction, which resulted in
327 the current directions are depended on wind direction in both seasons. However, the current
328 directions are complex in a zone (top right corner in [Figure 9](#)), which can be attributed to a
329 complex topography and influences of river discharge. The seasonal variability of river
330 discharge and monsoon winds has a large influence on water stratification and destratification.
331 Furthermore, the seasonal occurrence of stratification has an effect on the sediment dynamics
332 and ecosystem processes.

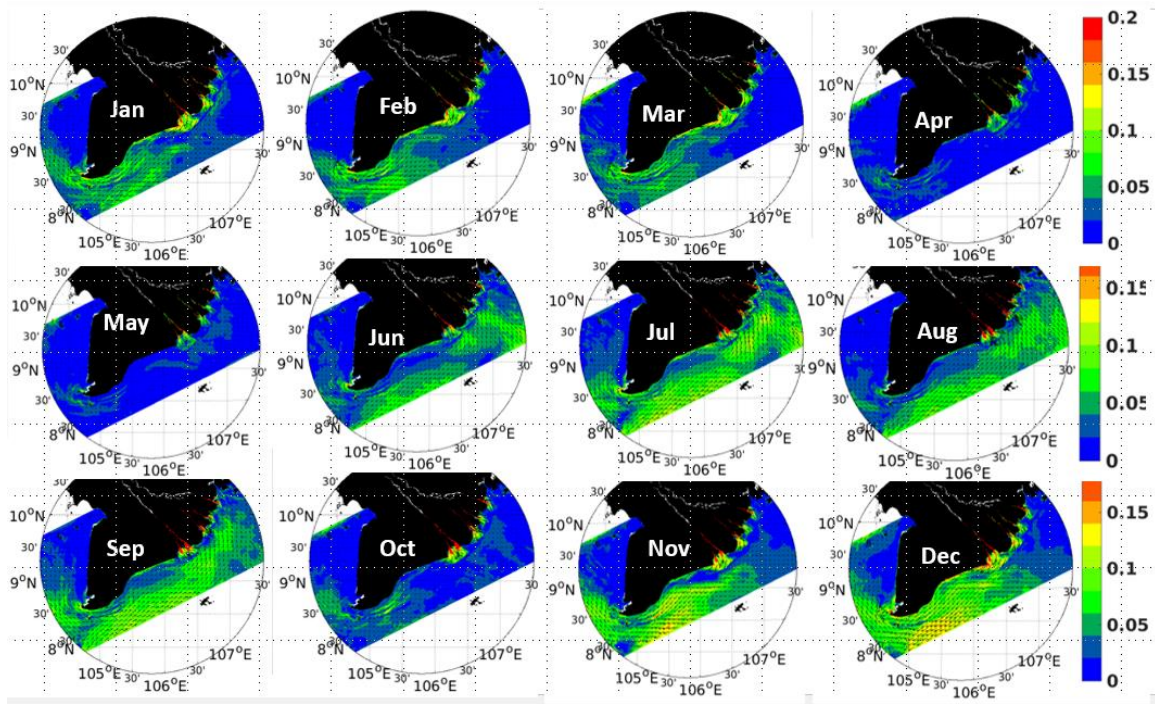


333

334

Figure 8. Monthly average surface velocity fields (m/s) in 2014.

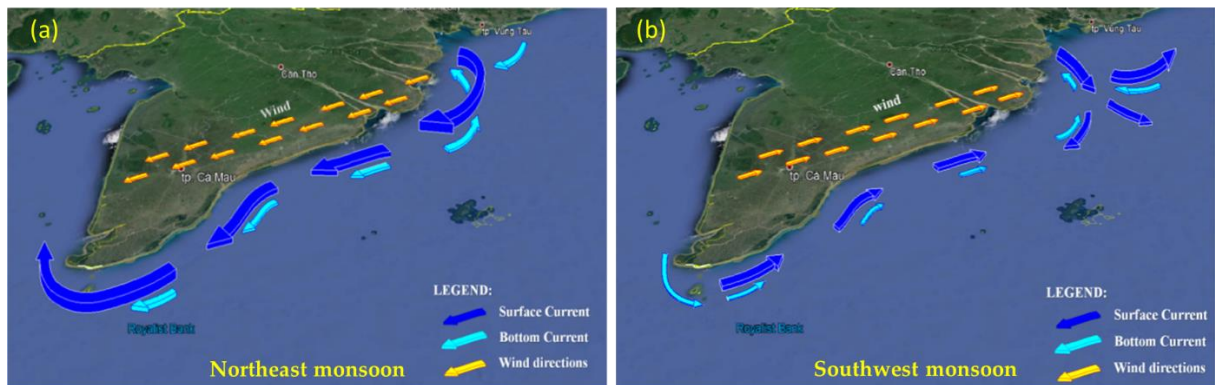
335



336

337

Figure 9. Monthly average bottom velocity fields (m/s) in 2014.



338

339

340

341

342

343

344

Figure 10. Proposed conceptual model of the coastal flow structure in the LMDCZ. (a) during the Northeast monsoon, wind stimulates downwelling-surface narrow jet of about 20-40 km of width and 5 m of thickness, and during the SW monsoon (b), wind simulates upwelling process.

5.3. Suspended sediment transport in the Mekong Delta

345

346

347

Figure 11 illustrates the monthly average suspended sediment fluxes for 10 sections (Figure 7A) of the LMDCZ in 2014, with those sections depicted in figure for the month of January. As expected, near the mouth of the Mekong Delta, the SSF increases from June to September,

348 which corresponds to the wet season when the river discharge and hence the sediment load are
349 highest. At the cross-section located northeast of the Dinh An and Tran De mouths (Figure 11),
350 the SSF can reach up to $2.25\text{-}2.40 \times 10^6$ tons/month. As time pass by, more suspended sediments
351 are transported by currents in a south-westerly direction from the mouth of the Mekong Delta
352 toward to the Ca Mau Cape. At the cross-section located southwest, just after the Dinh An
353 mouth, SSF increases from a value of 2.30×10^6 tons/month in October, to reach the highest
354 value of 6.36×10^6 tons/month in December. During this month, SSFs are the highest of the year
355 for all coastal sections. In the East Sea, offshore from the Ca Mau Cape, SSF reaches a value
356 of 5.32×10^6 tons/month and goes into the West Sea with a value of 5.89×10^6 tons/month. SSF
357 decrease from January to March and during the inter-season (April and May), SSF is nearly
358 insignificant. The analysis of the sediment budget was calculated for the 10 sections of the
359 LMDCZ mentioned above, with Table 2A presenting the sediment budget for each of those
360 sections as estimated by the CROCO model, with negative and positive values representing
361 zones of erosion and accretion, respectively. The zones of erosion and accretion, as determined
362 by the model are also depicted in Figure 12. It can be seen that sections S2, S4, and S9 have
363 experienced erosion according to the model (Figure 7A), which agrees with the observed
364 shoreline changes observed from 1990 to 2015 also show agreement between the model and
365 observations for section S3, S4, and S9 (Marchesiello *et al.* 2019). In section S3, erosion area
366 is calculated for the East Sea before the Ca-Mau Cape, an accretion area just behind it in the
367 West Sea, and then an erosion area in the North of the section. Thus, this makes the sediment
368 budget in this cell negative. Section S4, corresponding to the Ganh-Hao zone, is eroding during
369 most months with a sediment budget of -7.02×10^6 tons. Section S9, corresponding to the Go
370 Cong zone, is eroding during the Northeast winds from October to May, with a sediment budget
371 of -1.94×10^6 tons. According to Table 4 section S2, which extends from the Ca Mau Cape
372 experiences accretion, in agreement with observations. Section S1 in the West Sea is
373 experiencing erosion according to observations, but this is not seen in the model simulation.

374 The yearly computed sediment budget of this section is almost null, i.e., no erosion nor
375 accretion occurs. The reason for this disagreement is likely because of the impact of subsidence
376 with a rate of 20 mm/year in this area, the highest in the LMD, which is not yet taken into
377 consideration by the CROCO model.

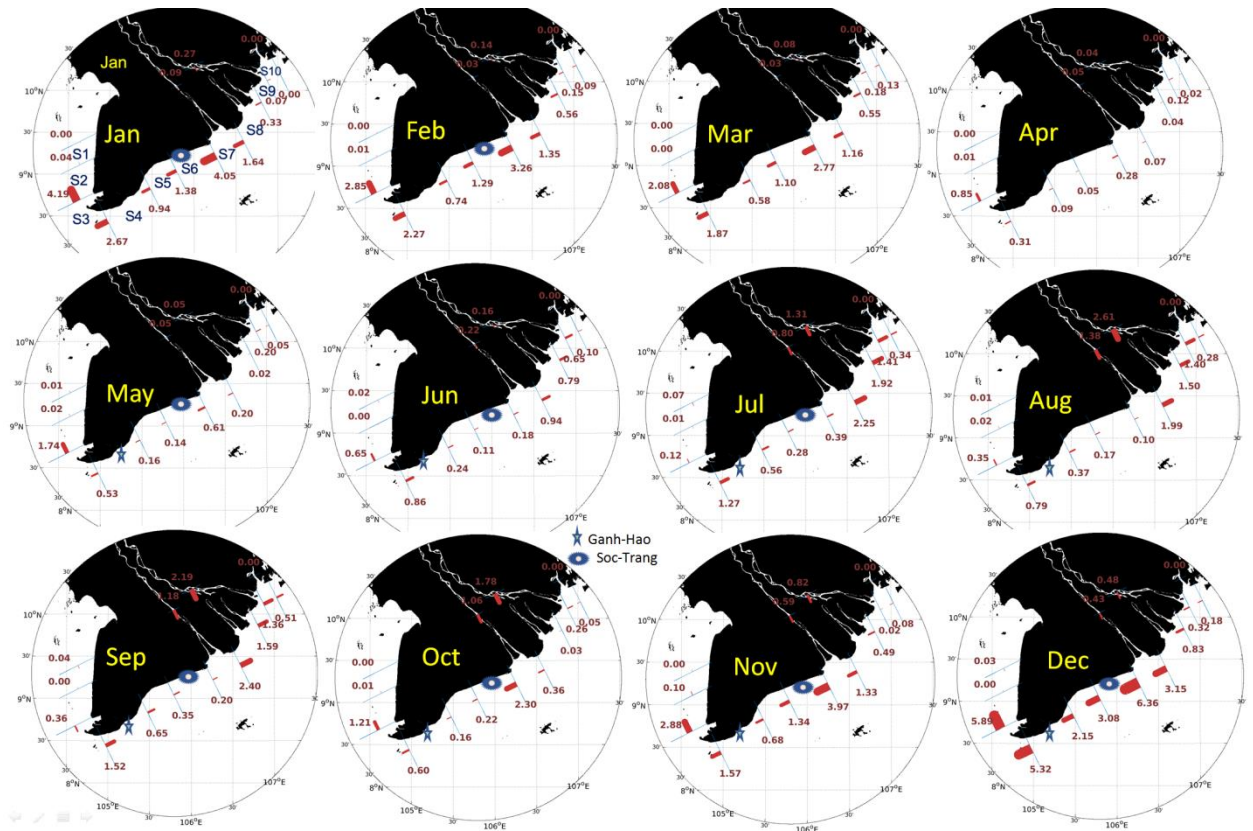
378

379 [Hein et al. \(2013\)](#) modelled the dynamics of sediments in the ROFI of the Mekong Delta and,
380 as in [Hordoir et al. \(2006\)](#), confirmed the important role that the seasonal cycle of river
381 discharge and monsoonal winds play on the Mekong Delta; their study, however, focused on
382 sediment deposition and not on the characteristics of the freshwater plume. Previous studies
383 have shown the deposition of fine sediments over the continental shelf during the SW monsoon
384 season due to high river discharge. Their model further suggests that sediment deposition also
385 occurs during the low flow season, but it is limited to areas near the river mouth, where the
386 delta is still expanding, and that the wind driven circulation, waves, and tidal action cause net
387 erosion in other parts of the Lower Mekong Delta Coastal Zone. Even though the net transport
388 of fine sediments is to the south, i.e., towards the Gulf of Thailand, in the southern part of the
389 delta, there is a negative sediment budget due to the strong coastal current causing coastal
390 erosion and hence shoreline retreat, evidence for which is presented in [Karlsruud et al. \(2017\)](#).
391 This strong coastal current during the northeast winter monsoon, flowing in the direction of the
392 propagating Kelvin wave, was also observed in the modelling study of [Hordoir et al. \(2006\)](#).

393

394 [Hein et al. \(2013\)](#) recommended further studies to examine the influence of hydropower dams
395 in the upper catchment of the Mekong River as well as the impacts of climate change. This was
396 also stressed more recently by [Li et al. \(2017\)](#) who mentioned that our understanding of the
397 evolution of the delta over the past 50 years is not adequate to respond to the impacts of climate
398 change. Accordingly, they used Landsat data over the period 1973-2015 and found that the
399 majority of the delta is experiencing erosion, particularly to the East of the Ca Mau Peninsula

400 and the north-western side of the delta in the Gulf of Thailand and that overall, the Mekong
 401 Delta has experienced a shift from a growing to a shrinking region around the year 2005.



402

403 **Figure 12.** Monthly average suspended sediment fluxes (10^6 tons/month) at different cross-
 404 sections of the LMDCZ

405 **6. Conclusions**

406 In this study, the three-dimensional CROCO model was used to simulate the circulation and
 407 transport of sediments in the ROFI of the Mekong Delta. The model was validated using *in situ*
 408 measurements, including significant wave height, tidal levels, and salinity profiles. The flow
 409 structure obtained using a 30-layer vertical grid closely agrees with the conceptual model
 410 proposed in relation to conditions either favouring upwelling or downwelling under seasonally
 411 varying wind direction. During the SW monsoon when the winds are favourable to upwelling,
 412 large volumes of freshwater flow out of the various rivers flowing into the Mekong Delta. When
 413 the North-eastern winds prevail, which favour downwelling, Ekman transport pushes the
 414 current against the coast, resulting in a narrow surface coastal jet, 25-40 km wide and 5 m thick.

415 This coastal jet allows for the transportation of suspended sediments toward the Ca Mau Cape
416 and further into the West Sea.

417

418 A sediment budget analysis was performed to identify zones prone to accretion and erosion in
419 the coastal zone of the LMD and to inform the development of preventive actions against
420 coastal erosion and the wider integrated coastal management agenda in the region. The results
421 of this analysis showed good agreement with an erosion map obtained from the Southern
422 Institute of Water Resources Research (SIWRR), confirming the suitability of the model for
423 further simulation. It is recommended that the model be used in further research to simulate the
424 impacts of different scenarios of changes in river discharge due to anthropogenic alterations of
425 the river flow or as a result of climate change, sand mining and sea level rise on the processes
426 and dynamics of the ROFI and sediment transport in the delta.

427

428 **Authorship statement**

429 Nguyet-Minh Nguyen, Dinh Cong San, Kim Dan Nguyen: Conceptualization, Methodology,
430 Software, Validation, Visualisation, Formal analysis, Investigation, Original draft preparation.

431 Quoc Bao Pham, Alexandre S. Gagnon, Duong Tran Anh: Supervision, Conceptualization,
432 Methodology, Final draft preparation, reviewing and Editing.

433 **Declaration of competing interest**

434 The authors reported no potential competing interest

435 **Acknowledgments**

436 The results presented in this paper were obtained as part of the LMDCZ Project financed by the
437 *Agence Française de Développement (AFD)* and the European Union. We would like to thank
438 the VITEL project team for sharing the CTD measurements. We also thank the Fulbright U.S.

439 – ASIAN visiting scholar program (G-1-00005) for awarding a research exchange to Dr Duong
440 Tran Anh at the University of South Florida, USA, in the summer of 2021. The authors greatly
441 appreciate the Editor and also deeply thank the anonymous reviewers for their constructive
442 comments to improve the final version of the manuscript.

443

444 **References**

445 Anthony, E.J., Brunier, G., Besset, M., Goichot, M., Dussouillez, P., Nguyen, V.L., 2015. Linking rapid
446 erosion of the Mekong river delta to human activities. *Sci. Rep.* 5, 14745.

447 Avicola, G. and Huq, P., 2003a. The characteristics of the recirculating bulge region in coastal buoyant
448 outflows. *Journal of Marine Research*, 61(4), pp.435-463.

449 Avicola, G. and Huq, P., 2003b. The role of outflow geometry in the formation of the recirculating bulge
450 region in coastal buoyant outflows. *Journal of marine research*, 61(4), pp.411-434.

451 Blaas, M., Dong, C., Marchesiello, P., McWilliams, J.C. and Stolzenbach, K.D., 2007. Sediment-
452 transport modeling on Southern Californian shelves: A ROMS case study. *Continental shelf
453 research*, 27(6), pp.832-853.

454 Boretti, A., 2020. Implications on food production of the changing water cycle in the Vietnamese
455 Mekong Delta. *Global Ecology and Conservation*, 22, p.e00989.

456 Buschmann, J., Berg, M., Stengel, C., Winkel, L., Sampson, M.L., Trang, P.T.K. and Viet, P.H., 2008.
457 Contamination of drinking water resources in the Mekong delta floodplains: Arsenic and other trace
458 metals pose serious health risks to population. *Environment International*, 34(6), pp.756-764.

459 Campbell, I.C., 2012. Biodiversity of the Mekong delta. In *The Mekong Delta System* (pp. 293-313).
460 Springer, Dordrecht.

461 Chao, S.-Y. 1990. Tidal modulation of estuarine plumes. *Journal of Physical Oceanography*, 20(7),
462 1115–1123.

463 Chen, C., Lai, Z., Beardsley, R.C., Xu, Q., Lin, H. and Viet, N.T., 2012. Current separation and
464 upwelling over the southeast shelf of Vietnam in the South China Sea. *Journal of Geophysical Research:
465 Oceans*, 117(C3).

466 Cochran, T.A., Arias, M.E. and Piman, T., 2014. Historical impact of water infrastructure on water
467 levels of the Mekong River and the Tonle Sap system. *Hydrology and Earth System Sciences*, 18(11),
468 pp.4529-4541.

469 De Boer, G.J., Pietrzak, J.D. and Winterwerp, J.C., 2006. On the vertical structure of the Rhine region
470 of freshwater influence. *Ocean dynamics*, 56(3), pp.198-216.

471 de Kok, J.M. 1996. A two-layer model of the Rhine plume. *Journal of marine Systems*, 8, 269–284.

472 Debreu, L., Auclair, F., Benshila, R., Capet, X., Dumas, F., Julien, S. and Marchesiello, P., 2016, April.
473 Multiresolution in CROCO (Coastal and Regional Ocean Community model). In *EGU General*
474 *Assembly Conference Abstracts* (pp. EPSC2016-15272).

475 Debreu, L., Marchesiello, P., Penven, P. and Cambon, G., 2012. Two-way nesting in split-explicit ocean
476 models: Algorithms, implementation and validation. *Ocean Modelling*, 49, pp.1-21.

477 Dong, J., Fox - Kemper, B., Zhu, J. and Dong, C., 2021. Application of symmetric instability
478 parameterization in the Coastal and Regional Ocean Community Model (CROCO). *Journal of*
479 *Advances in Modeling Earth Systems*, 13(3), p.e2020MS002302.

480 Fong, D.A. and Geyer, W.R., 2001. Response of a river plume during an upwelling favorable wind
481 event. *Journal of Geophysical Research: Oceans*, 106(C1), pp.1067-1084.

482 Fong, D.A. and Geyer, W.R., 2002. The alongshore transport of freshwater in a surface-trapped river
483 plume. *Journal of Physical Oceanography*, 32(3), pp.957-972.

484 Garcia Berd'eal, I., Hickey, B.M., & Kawase, M. 2002. Influence of wind stress and ambient
485 Geyer, W., and G. Kineke. 1995. Observations of currents and water properties in the Amazon frontal
486 zone, *J. Geophys. Res.*, 100, 2321–2339.

487 Geyer, W.R., Signell, R.P., Fong, D.A., Wang, J., Anderson, D.M. and Keafer, B.A., 2004. The
488 freshwater transport and dynamics of the western Maine coastal current. *Continental Shelf*
489 *Research*, 24(12), pp.1339-1357.

490 Guong, V.T. and Hoa, N.M., 2012. Aquaculture and agricultural production in the Mekong Delta and
491 its effects on nutrient pollution of soil and water. In *The Mekong Delta System* (pp. 363-393). Springer,
492 Dordrecht.

493 Hein, B., 2013. Processes of stratification and destratification in the Mekong ROFI-seasonal and
494 intraseasonal variability (Doctoral dissertation, Staats-und Universitätsbibliothek Hamburg Carl von
495 Ossietzky).

496 Hein, H., Hein, B. and Pohlmann, T., 2013. Recent sediment dynamics in the region of Mekong water
497 influence. *Global and Planetary Change*, 110, pp.183-194.

498 Hickey, B.M., Pietrafesa, L.J., Jay, D.A. and Boicourt, W.C., 1998. The Columbia River plume study:
499 Subtidal variability in the velocity and salinity fields. *Journal of Geophysical Research:*
500 *Oceans*, 103(C5), pp.10339-10368.

501 Hordoir, R., Nguyen, K.D. and Polcher, J., 2006. Simulating tropical river plumes, a set of
502 parametrizations based on macroscale data: A test case in the Mekong Delta region. *Journal of*
503 *Geophysical Research: Oceans*, 111(C9).

504 Horner-Devine, A.R., Hetland, R.D. and MacDonald, D.G., 2015. Mixing and transport in coastal river
505 plumes. *Annual Review of Fluid Mechanics*, 47, pp.569-594.

506 Horner-Devine, A.R., Jay, D.A., Orton, P.M. and Spahn, E. Y., 2009. A conceptual model of the strongly
507 tidal Columbia River plume. *Journal of Marine Systems*, 78(3), pp.460-475.

508 IRD, “Franco-Vietnamese Oceanographic Campaigns with the ALIS Research Vessel of the French
509 Institute of Research for Development - June 19 to July 12, 2014,” *Final Report*, 2014.

510 Joseph, A., 2017. Investigating Seafloors and Oceans: From Mud Volcanoes to Giant Squid. Elsevier.
511 <https://doi.org/10.1016/C2015-0-05842-7>

512 Karlsrud, K., Vangelsten, B.V. and Frauenfelder, R., 2017. Subsidence and shoreline retreat in the Ca
513 Mau Province–Vietnam. Causes, consequences and mitigation options. *Geotechnical Journal of the*
514 *SEAGS & AGSSEA*, 48.

515 Kondolf, G.M., Rubin, Z.K. and Minear, J.T., 2014. Dams on the Mekong: Cumulative sediment
516 starvation. *Water Resources Research*, 50(6), pp.5158-5169.

517 Large, W.G., McWilliams, J.C. and Doney, S.C., 1994. Oceanic vertical mixing: A review and a model
518 with a nonlocal boundary layer parameterization. *Reviews of geophysics*, 32(4), pp.363-403.

519 Le Xuan, T., Thanh, V.Q., Reyns, J., Van, S.P., Anh, D.T., Dang, T.D. and Roelvink, D., 2019.
520 Sediment transport and morphodynamical modeling on the estuaries and coastal zone of the Vietnamese
521 Mekong Delta. *Continental Shelf Research*, 186, pp.64-76.

522 Li, X., Liu, J.P., Saito, Y. and Nguyen, V.L., 2017. Recent evolution of the Mekong Delta and the
523 impacts of dams. *Earth-Science Reviews*, 175, pp.1-17.

524 Marchesiello, P., McWilliams, J.C. and Shchepetkin, A., 2001. Open boundary conditions for long-
525 term integration of regional oceanic models. *Ocean Modelling*, 3(1-2), pp.1-20.

526 Marchesiello, P., Nguyen, N.M., Gratiot, N., Loisel, H., Anthony, E.J., San Dinh, C., Nguyen, T.,
527 Almar, R. and Kestenare, E., 2019. Erosion of the coastal Mekong delta: Assessing natural against man
528 induced processes. *Continental Shelf Research*, 181, pp.72-89.

529 Meade, R.H., 1996. River-Sediment Inputs to Major Deltas. In: J.D. Milliman and B.U. Haq (Editors),
530 Sea-Level Rise and Coastal Subsidence: Causes, Consequences, and Strategies. Springer Netherlands,
531 Dordrecht, pp. 63-85.

532 Minderhoud, P.S.J., Erkens, G., Pham, V.H., Bui, V.T., Erban, L., Kooi, H., Stouthamer, E., 2017.
533 Impacts of 25 years of groundwater extraction on subsidence in the Mekong delta, Vietnam.
534 *Environmental Research Letters* 12(6), 064006.

535 Nhan, N.H. and Cao, N.B., 2019. Damming the Mekong: Impacts in Vietnam and solutions. In *Coasts*
536 *and Estuaries* (pp. 321-340). Elsevier.

537 Pardo, P.C., Padín, X.A., Gilcoto, M., Farina-Busto, L. and Pérez, F.F., 2011. Evolution of upwelling
538 systems coupled to the long-term variability in sea surface temperature and Ekman transport. *Climate*
539 *Research*, 48(2-3), pp.231-246.

540 Pimenta, F.M. and Kirwan Jr, A.D., 2014. The response of large outflows to wind forcing. *Continental*
541 *Shelf Research*, 89, pp.24-37.

542 Pimenta, F.M., Kirwan Jr, A.D. and Huq, P., 2011. On the transport of buoyant coastal plumes. *Journal*
543 *of Physical Oceanography*, 41(3), pp.620-640.

544 Price, J.F., Weller, R.A. and Schudlich, R.R., 1987. Wind-driven ocean currents and Ekman
545 transport. *Science*, 238(4833), pp.1534-1538.

546 Rubin, Z.K., Kondolf, G.M., Carling, P.A., 2015. Anticipated geomorphic impacts from Mekong basin
547 dam construction. *International Journal of River Basin Management* 13(1), 105-121.

548 Sarmiento, J.L. and Gruber, N., 2006. *Ocean biogeochemical dynamics*. Princeton University Press.
549 [ISBN 978-0-691-01707-5](#)

550 Schmidt, C., 2015. Alarm over a sinking delta. *Science* 348(6237), 845-846

551 Shchepetkin, A.F. and McWilliams, J.C., 2003. A method for computing horizontal pressure - gradient
552 force in an oceanic model with a nonaligned vertical coordinate. *Journal of Geophysical Research:*
553 *Oceans*, 108(C3).

554 Shchepetkin, A.F. and McWilliams, J.C., 2005. The regional oceanic modeling system (ROMS): a split-
555 explicit, free-surface, topography-following-coordinate oceanic model. *Ocean modelling*, 9(4), pp.347-
556 404.

557 Simpson, J. H. and A. Snidvongs, 1998. The influence of monsoonal river discharge on tropical shelf
558 seas: the Gulf of Thailand as a case for study. Proceedings of the International Workshop on the Mekong
559 Delta at Chiang Rai on 23–27 February 1998, 86–99.

560 Simpson, J.H., 1997. Physical processes in the ROFI regime. *Journal of marine systems*, 12(1-4), pp.3-
561 15.

562 Simpson, J.H., Williams, E., Brasseur, L.H. and Brubaker, J.M., 2005. The impact of tidal straining on
563 the cycle of turbulence in a partially stratified estuary. *Continental Shelf Research*, 25(1), pp.51-64.

564 Smajgl, A., Toan, T.Q., Nhan, D.K., Ward, J., Trung, N.H., Tri, L.Q., Tri, V.P.D., Vu, P.T., 2015.
565 Responding to rising sea levels in the Mekong Delta. *Nature Climate Change* 5(2), 167-174

566 Soufflet, Y., Marchesiello, P., Lemarié, F., Jouanno, J., Capet, X., Debreu, L. and Benshila, R., 2016.
567 On effective resolution in ocean models. *Ocean Modelling*, 98, pp.36-50.

568 Southern Institute of Water Resources Research (SIWRR). 2018. Erosion processes in the Lower
569 Mekong Delta Coastal Zones and measures for protecting Go-Cong and Phu-Tan, Final Report, AFD,
570 Vietnam.

571 Thanh, V.Q., Reyns, J., Wackerman, C., Eidam, E.F. and Roelvink, D., 2017. Modelling suspended
572 sediment dynamics on the subaqueous delta of the Mekong River. *Continental Shelf Research*, 147,
573 pp.213-230.

574 Thomas, P.J. and Linden, P.F., 2010. Laboratory modelling of the effects of temporal changes of
575 estuarine-fresh-water discharge rates on the propagation speed of oceanographic coastal
576 currents. *Journal of fluid mechanics*, 664, p.337.

577 Wang, D., Wang, H., Li, M., Liu, G. and Wu, X., 2013. Role of Ekman transport versus Ekman pumping
578 in driving summer upwelling in the South China Sea. *Journal of Ocean University of China*, 12(3),
579 pp.355-365.

580 Warner, J.C., Sherwood, C.R., Signell, R.P., Harris, C.K. and Arango, H.G., 2008. Development of a
581 three-dimensional, regional, coupled wave, current, and sediment-transport model. *Computers &*
582 *geosciences*, 34(10), pp.1284-1306.

583 Whitney, M.M. and Garvine, R.W., 2005. Wind influence on a coastal buoyant outflow. *Journal of*
584 *Geophysical Research: Oceans*, 110(C3).

585 Wolanski, E., Huan, N.N., Nhan, N.H. and Thuy, N.N., 1996. Fine-sediment dynamics in the Mekong
586 River estuary, Vietnam. *Estuarine, Coastal and Shelf Science*, 43(5), pp.565-582.

587 Xing, J. and Chen, S., 2017. A process study of the interaction of tidal currents, tidal mixing and density
588 gradients in a region of freshwater influence. *Journal of Marine Systems*, 172, pp.51-63.

589 Yankovsky, A.E., Hickey, B.M. and Münchow, A.K., 2001. Impact of variable inflow on the dynamics
590 of a coastal buoyant plume. *Journal of Geophysical Research: Oceans*, 106(C9), pp.19809-19824.

591 Yao, H.Y., Leonardi, N., Li, J.F. and Fagherazzi, S., 2016. Sediment transport in a surface-advected
592 estuarine plume. *Continental Shelf Research*, 116, pp.122-135.

593 Yuan, Y., Horner-Devine, A.R., Avenir, M. and Bevan, S., 2018. The role of periodically varying
594 discharge on river plume structure and transport. *Continental Shelf Research*, 158, pp.15-25.

595 Ziv, G., Baran, E., Nam, S., Rodríguez-Iturbe, I. and Levin, S.A., 2012. Trading-off fish biodiversity,
596 food security, and hydropower in the Mekong River Basin. *Proceedings of the National Academy of*
597 *Sciences*, 109(15), pp.5609-5614.

598 Johnson, G.C., Schmidtko, S. and Lyman, J.M., 2012. Relative contributions of temperature and salinity
599 to seasonal mixed layer density changes and horizontal density gradients. *Journal of Geophysical*
600 *Research: Oceans*, 117(C4).

601 Chaufray, J.Y., Gonzalez-Galindo, F., Forget, F., Lopez-Valverde, M., Leblanc, F., Modolo, R., Hess,
602 S., Yagi, M., Bletly, P.L. and Witasse, O., 2014. Three-dimensional Martian ionosphere model: II. Effect

603 of transport processes due to pressure gradients. *Journal of Geophysical Research: Planets*, 119(7),
604 pp.1614-1636.
605
606
607

608 **Supplementary data (Appendix).**

609 **Table 1A.** Seasonal variations in prevailing winds over the Mekong Delta and associated
 610 climatic conditions.

| | | | | | | | | | | | | |
|--------------|-----|-----|-------------|-----|-----|------------|-----|-----|-----|----------------|--------------|--|
| Cool and dry | | | Hot and dry | | | Wet | | | | | Cool and dry | |
| Jan | Feb | Mar | Apr | May | Jun | Jul | Aug | Sep | Oct | Nov | Dec | |
| NE Monsoon | | | Transition | | | SW Monsoon | | | | Trans ition | NE Monsoon | |

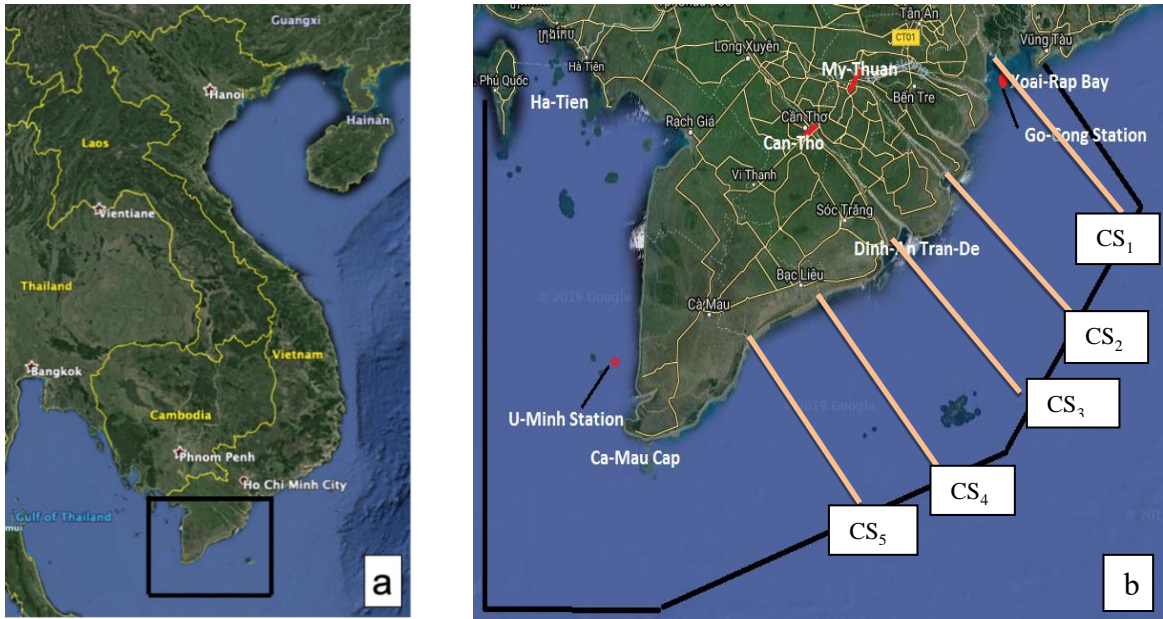
611
 612

613 **Table 2A.** Monthly sediment budget (10^6 tons) in the different sections of the LMDCZ (see
 614 Figure – January - for their position) estimated by the CROCO model in 2014.

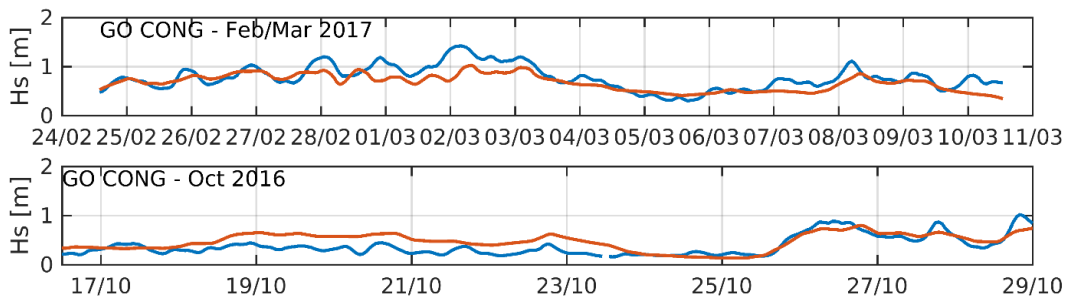
| | Jan | Feb | Mar | Apr | May | Jun | Jul | Aug | Sep | Oct | Nov | Dec | Sum |
|------------|-------|-------|-------|-------|-------|-------|-------|-------|-------|-------|-------|-------|--------|
| S1 | 0.04 | 0.01 | -0.01 | 0.01 | 0.02 | 0.03 | 0.06 | 0.01 | 0.06 | 0.01 | 0.10 | 0.04 | 0.37 |
| S2 | 4.16 | 2.85 | 2.09 | 0.84 | 1.72 | 0.65 | 0.15 | 0.33 | -0.38 | 1.21 | 2.78 | 5.89 | 22.28 |
| S3 | -1.53 | -0.58 | -0.21 | -0.54 | -1.22 | -1.51 | -1.41 | -1.15 | -1.16 | -0.61 | -1.31 | -0.56 | -11.79 |
| S4 | -1.72 | -1.53 | -1.29 | -0.22 | -0.37 | 0.61 | 0.72 | 0.42 | 0.87 | -0.44 | -0.89 | -3.18 | -7.02 |
| S5 | 0.43 | 0.54 | 0.52 | -0.04 | -0.02 | 0.14 | 0.28 | 0.19 | 0.30 | 0.07 | 0.66 | 0.94 | 4.02 |
| S6 | 2.68 | 1.97 | 1.67 | 0.23 | 0.47 | -0.08 | -0.11 | 0.08 | 0.15 | 2.08 | 2.63 | 3.28 | 15.03 |
| S7 | 2.51 | 1.94 | 1.64 | 0.27 | 0.46 | 0.98 | 2.66 | 3.28 | 3.39 | 3.00 | 3.24 | 3.65 | 27.02 |
| S8 | 1.58 | 0.94 | 0.70 | 0.07 | 0.23 | 0.31 | 1.64 | 3.11 | 3.02 | 2.12 | 1.66 | 2.80 | 18.19 |
| S9 | -0.41 | -0.41 | -0.36 | -0.17 | -0.23 | 0.14 | 0.52 | 0.10 | 0.23 | -0.30 | -0.52 | -0.51 | -1.94 |
| S10 | 0.07 | -0.05 | -0.06 | 0.15 | 0.26 | 0.55 | 1.07 | 1.12 | 0.85 | 0.32 | 0.11 | -0.14 | 4.25 |

615

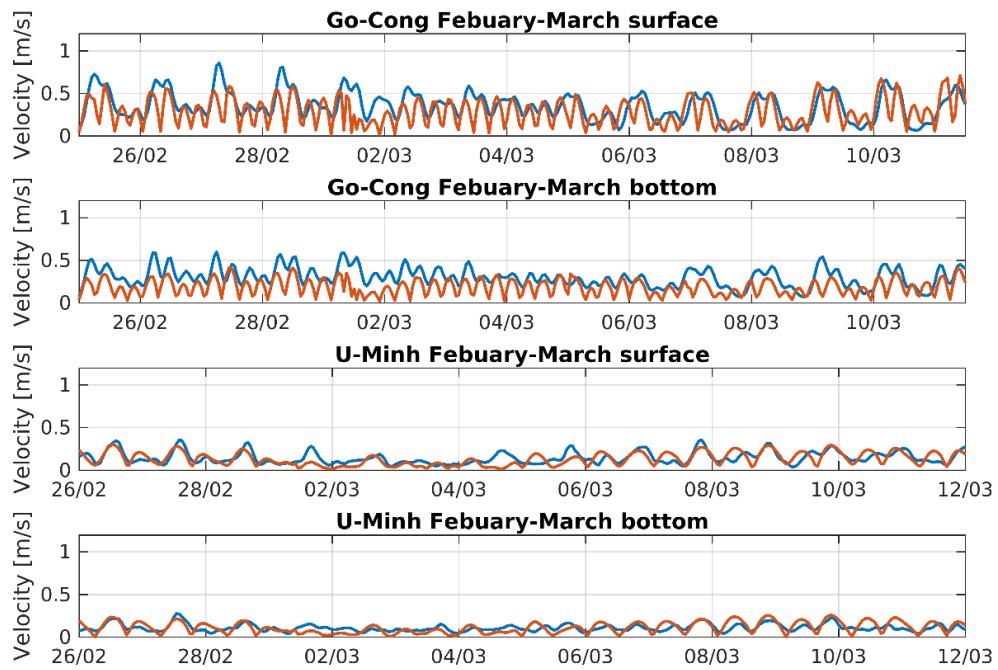
616



617 **Figure 1A.** a) Location of the LMDCZ and b) computational domain of the CROCO model
 618 over the Mekong Delta, showing the two upstream open boundaries at Can Tho and My Thuan,
 619 and the sea open boundaries at Go Cong and U Minh. CS₁₋₅ refer to the location of the five
 620 cross-sections referred to in the text.



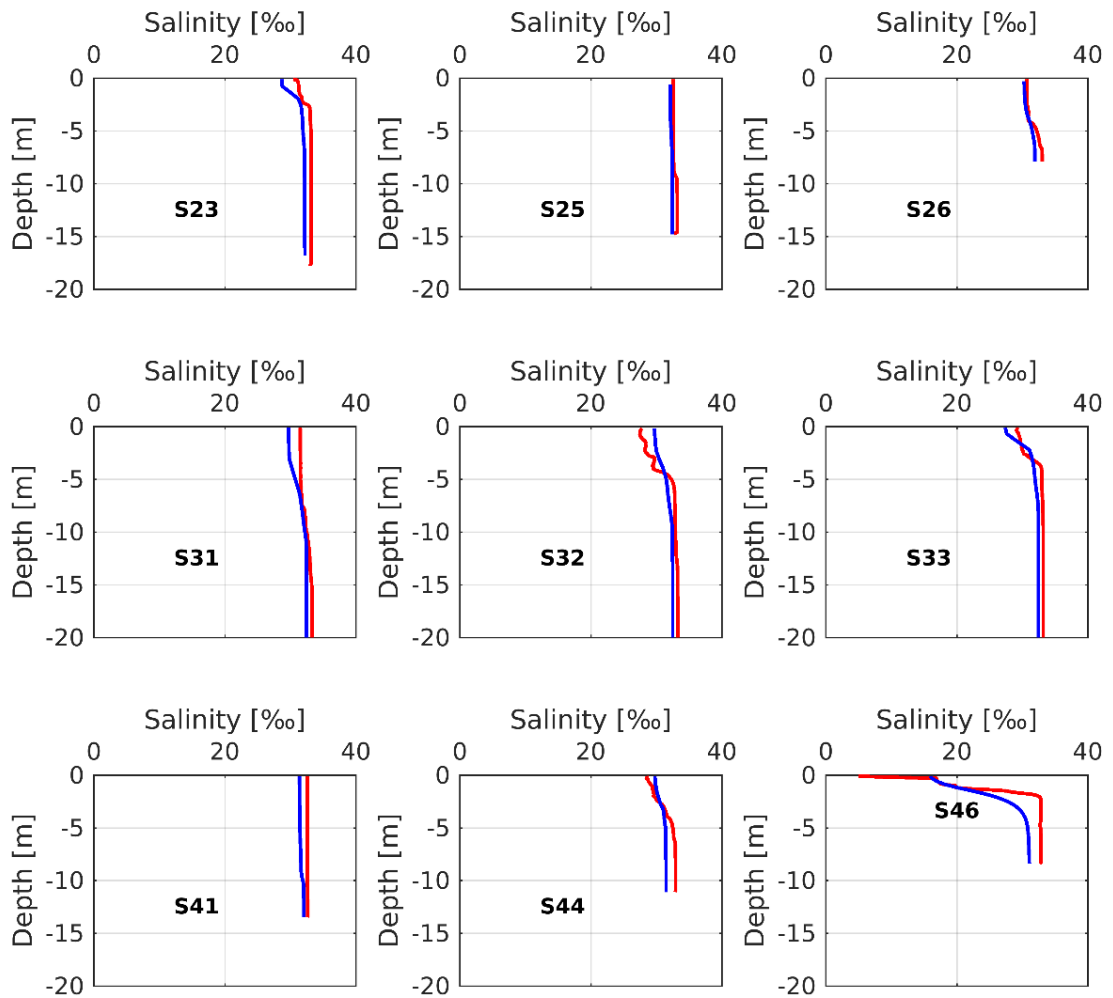
621
 622 **Figure 2A.** Significant wave height (Hs) as simulated by the model and observed at Go Cong
 623 during the 15-day field campaign extending from February 24 to March 11, 2017 (top panel),
 624 and the 15-day field campaign on October 16-31, 2016 (bottom panel).



625

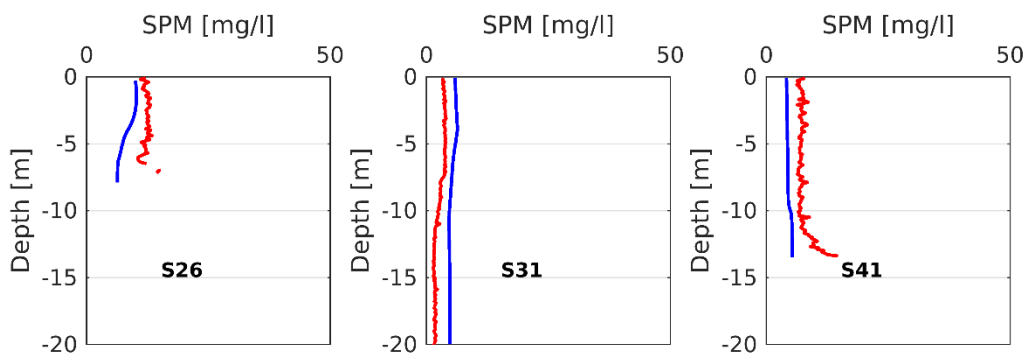
626 **Figure 3A.** Modelled and observed current velocity during the 15-day field campaign from
 627 February 24 to March 11, 2017, at the surface and the bottom of the sea at U Minh and Go
 628 Cong.

629

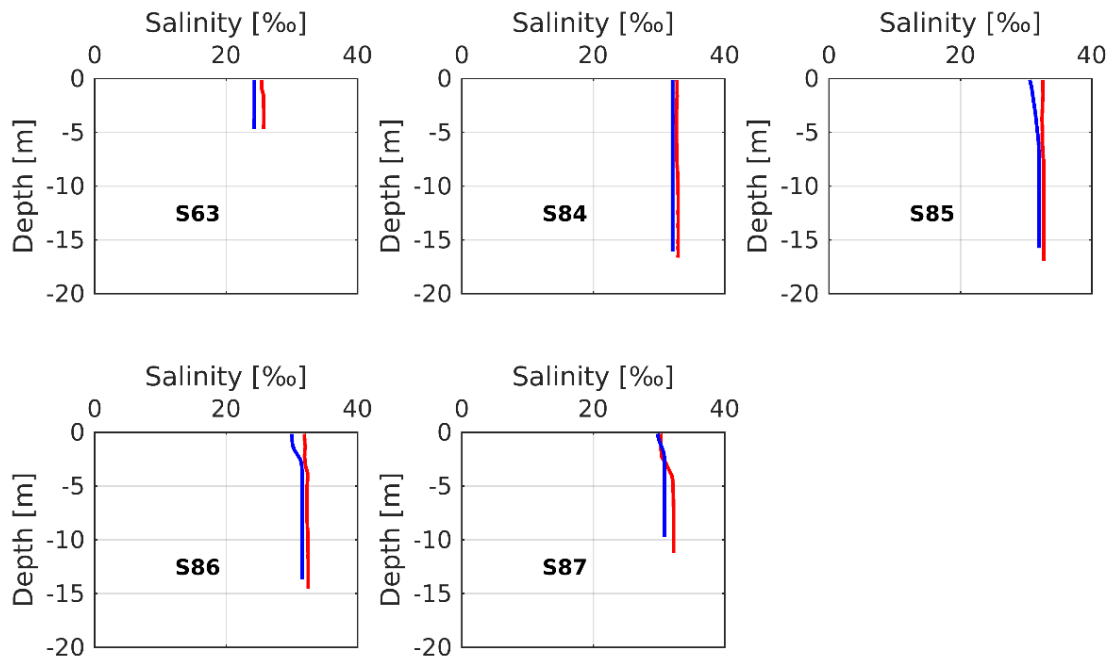


630

631 **Figure 4A.** Comparison of the salinity profile simulated (blue curves) and observed (red curves)
 632 during the field measurements taken as part of the VITEL project in June 2014 at different
 633 locations.



634



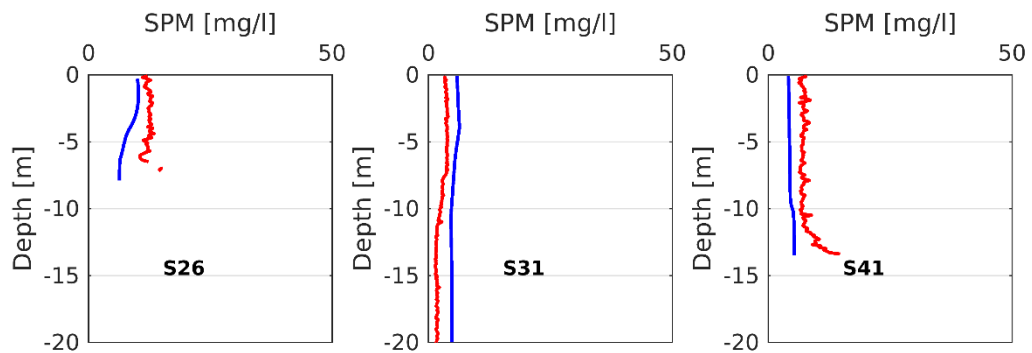
635

636 **Figure 5A.** Comparison of the salinity profile simulated (blue curves) and observed (red curves)

637 during the field measurements taken as part of the LMDCZ project in February-March 2017 at

638 different locations.

639

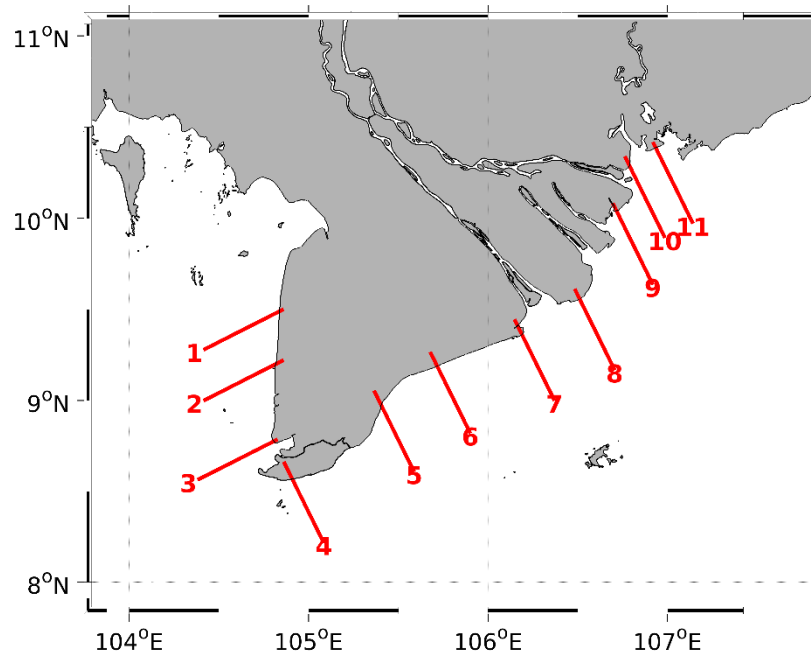


640

641 **Figure 6A.** Comparison of the instantaneous SPM profile simulated by the CROCO model

642 (blue curves) and observed in June 2014 by the VITEL project field measurements (red

643 curves).



644
645
646
647
648
649
650
651

Figure 7A. The location of ten sections (S1 – S10) for extracting suspended sediment fluxes